Journal of Electroanalytical Chemistry 963 (2024) 118325

Contents lists available at ScienceDirect

Journal of Electroanalytical Chemistry

journal homepage: www.elsevier.com/locate/jelechem

Cocoa husk as precursor of carbonaceous materials for supercapacitors electrodes

Lilian D. Ramírez-Valencia [a], Franz E. López-Suárez [b,*], Laura R. Conde [c], Esther. Bailón-García [a], Agustín Bueno-López [b], Agustín F. Perez-Cadenas [a]

[a] Materiales Polifuncionales Basados en Carbono (UGR-Carbon), Dpto. Química Inorgánica-Unidad de Excelencia Química Aplicada a Biomedicina y Medioambiente-Universidad de Granada (UEQ-UGR), ES18071 Granada, Spain
[b] MCMA Group, Department of Inorganic Chemistry, Faculty of Sciences, University of Alicante, Ap. 99 E-03080, Alicante, Spain
[c] Department of Chemical and Environmental Engineering, Universidad Nacional de Colombia, 111321 Bogotá D.C., Colombia

ARTICLE INFO

Keywords:
Activated carbon
Chemical activation
Pseudocapacitance
Electric double layer
Supercapacitor
Electrodes

ABSTRACT

Activated carbon materials are widely used as high-performance electrodes for supercapacitors because they allow improving the electrochemical performance of these devices. The development of high surface areas and high porosity contributes to the energy storage by double electric layer, whereas the content of different functional groups on their surface to the pseudocapacitive storage. In addition, they can be obtained from lignocellulosic wastes providing a novel and economic perspective for the development of carbon-based electrodes. In this work, activated carbons were synthesized from cocoa husks using KOH as activating agent. The materials were obtained at three impregnation ratios (1:1, 3:1, 5:1) and three carbonization temperatures (500, 650, and 800 °C), optimizing the best conditions to obtain materials with high surface areas and porosity together with surface functional groups to improve energy storage. The results show that the 800 °C synthesized material with 3:1 impregnation ratio presents a capacitance of 120 F/g at 1 A/g, with a retention capacity of 93 % after 12,000 cycles, being the best electrochemical behavior among the carbons prepared. This is attributed to the adequate micro-mesoporosity, content of surface oxygenated functional groups and high surface area (1444 m^2/g).

1. Introduction

The significant demands of energy have increased the production of clean and renewable energies from sunlight and wind, requiring the development of storage systems that allow taking advantage of the whole generated energy [1–3]. Electrochemical double-layer capacitors (EDLCs) or supercapacitors are devices that could store electrical energy in an electrochemical double–layer [4,5]. They have a higher power density than conventional capacitors, enabling good storage systems, [6] but suffer drawbacks mainly related to energy density. A latent alternative is the development of new materials with high specific surface areas and different surface functional groups that can be used to manufacture electrodes [7–9].

Carbonaceous materials are the most used materials for electrodes manufacture, and 80 % of commercially available supercapacitors are made of carbon [10]. Carbon nanotubes [11] mixed carbon aerogels, xerogels [12] and graphene materials [13,14] are commonly employed. Nevertheless, their production costs are high, representing a disadvantage for their application. Recently, active carbons obtained from lignocellulosic biomass have been studied, taking advantage of their high availability, low cost and low environmental impact [15,16].

Cocoa husk is a lignocellulosic material obtained after roasting the beans, representing between 12 %–20 % of cocoa beans, and is considered an industrial by-product or even a residue of the chocolate industry [17,18]. According to the International Cocoa Organization, the production of cocoa beans in 2021–2022 was about 4890 thousand tonnes, estimating a minimum coca shell production of around 617 thousand tons per year [19]. Thanks to its high carbon and low ashes contents [20], it could be a raw material for the obtention of suitable activated carbons for supercapacitor electrodes.

The main characteristics of activated carbons required for supercapacitor electrodes fabrication have been widely studied [21]. They are related to their high surface area (up to 1000 m^2/g), good electrolyte accessibility achieved by a well-developed pore-size distribution and

* Corresponding author.
E-mail addresses: liliandr@correo.ugr.es (L.D. Ramírez-Valencia), franz.lopez@ua.es, franzedwin@gmail.com (F.E. López-Suárez), lrconder@unal.edu.co (L.R. Conde), estherbg@ugr.es (Esther. Bailón-García), agus@ua.es (A. Bueno-López), afperez@ugr.es (A.F. Perez-Cadenas).

https://doi.org/10.1016/j.jelechem.2024.118325
Received 6 March 2024; Received in revised form 23 April 2024; Accepted 2 May 2024
Available online 3 May 2024

good conductivity. These properties allow adapting the size of the electrolyte ions and good physicochemical stability, providing materials with promising behavior as supercapacitors [22].

Different preparation methods are implemented to produce activated carbons with good textural properties and designed surface chemistry based on the activating agent and the synthesis conditions. Among the different methods, the chemical activation with different chemical agents, such as $ZnCl_2$, H_3PO_4, and KOH [23–28] are used. The activation using potassium hydroxide (KOH) as an oxidizing agent exhibits important advantages, since it implies lower activation energy, shorter activation times, and higher process yield. Moreover, activated carbons with well-developed microporosity and high surface area are obtained [29].

Several authors have reported different synthesis conditions and precursors, using temperatures between 500–800 °C and impregnation ratios from 0.25:1 to 5:1 (weight of KOH: weight of biomass) [30–36], concluding that it is necessary to tune the impregnation ratio and activation temperature. For instance, in the case of tobacco stems, an impregnation ratio of 0.5:1 (weight of KOH: weight of biomass) at an activation temperature of 600 °C allowed a maximum BET surface area of 500 $m^2.g^{-1}$ [37]. In the case of *Bambusa vulgaris striata,* the activation through a two-step process started with pyrolysis at 500 °C followed by impregnation using a 1:3 ratio (weight of KOH: weight of biomass) and a final activation at 800 °C, producing the highest surface area (980 m^2g^{-1}) [38]. The effect of activation temperature and impregnation ratio on the structural properties (surface area and porosity development) allow to obtain specific capacitances in the 178–355 F g^{-1} range.

Recently, Karakehya [39] evaluated two methodologies using KOH chemical activation to produce activated carbons from spores of *Lycopodium Clavatum* for energy storage. In this work was found that the synthesis method affects the electrochemical performance, which is directly related with well-developed micro-mesoporosity and high surface area. Jiang et al [40] used a two-step process involving precarbonization at 380 °C in air, followed by KOH activation at 700 °C to produce an optimum material with a specific surface area of 2372 m^2g^{-1} and an ultra-high capacitance of 290 Fg^{-1} at 1 Ag^{-1} in a two-electrode device with exceptional holding capacity.

The electrochemical behavior of lignocellulosic residues-derived materials can be also related to surface chemistry. For instance, capacitance values of 225 Fg^{-1}, 279 $Fg^{-1}$and 187 Fg^{-1} have been reported for rapeseed [41], willow catkins [32], and walnut shells [42], and have been related to the presence of surface oxygen heteroatoms. Oxygen improves the electrolyte wettability and favors their pseudocapacitance [32]. However, not all oxygenated functional groups contribute to the electrochemical response improvement. Martínez-Casillas et al (2019) found that oxygen functional groups that release CO upon decomposition favor the storage, while CO_2 releasing functional groups do not allow the delocalization of the electrons and reduce electrical conductivity and consequently the capacitance [43].

The procedure, synthesis parameters (temperature, activating agent and impregnation ratios) and lignocellulosic source have direct influence in the surface chemistry and electrochemical performance. Therefore, this work explores the use of cocoa husk (exploring a new raw material) as a precursor for the elaboration of active carbons and their use as electrodes for supercapacitors. This study aimed to prepare activated carbons from cocoa shells produced in high quantities in Colombia and evaluate their electrochemical performance. It is known that activating agents and pyrolysis temperature could affect the activation process and consequently the properties of the final activated carbon. The selection of interval of temperature and impregnation ratios were based on values reported in the literature for lignocellulosic waste, since the cocoa husk has not yet been explored as electrodes in supercapacitors. Low temperature combined with different impregnation ratios allow to obtain appropriate chemical – physical properties, as well as an increase in temperature combined with different impregnation ratios, should be considered to improve properties such as surface area, porosity, and surface chemical composition. Therefore, three temperatures ranging from 500 °C to 850 °C and varying KOH/material impregnation ratios from 1:1 to 1:5 are investigated. Special attention is paid to the impact that these synthesis conditions have on the surface chemistry of the activated carbons. The prepared materials were characterized to establish the relation between chemical-physical properties and the electrochemical response.

2. Experimental

2.1. Preparation of activated carbons

The cocoa husk was collected after the roasting process of the dried fruit generated by Nacional de Chocolates S.A.S company (Colombia). The cocoa husk was washed with deionized water, dried at 60 °C until constant weight and finally milled and sieved to achieve a particle size of 1 mm.

Cocoa husk was mixed with KOH at mass impregnation ratios (KOH: precursorwaste) of 1:1, 3:1 and 5:1 for 2 h at 45 °C. Afterward, the samples were pyrolyzed in a tube furnace under N_2 flow (50 ml/min) at 5 °C/min to the final temperature of 550, 650 or 800 °C, keeping this temperature for one hour. Finally, the prepared activated carbons were washed with HCl (1 M) and deionized water until 7pH and until no chloride ions were detected in the washing water (using a silver nitrate solution) and dried at 100 °C for 24 h. The samples prepared were named CC-X-Y, where X and Y denote samples pyrolysis temperature and impregnation ratio, respectively.

2.2. Physical-chemical characterization

The textural characterization for materials prepared was assessed by the adsorption of N_2 (−196 °C) and CO_2 (°C) in a Quantachrome Autosorb device. The samples were degassed at 110 °C for 8 h under vacuum (10^{-6} mbar). The results were processed through the Brunauer-Emmett-Teller (BET) equation to determine the BET surface area and micropore volume (W_0) and Dubinin Radushkevich (DR) for narrow volume micropore (L_0). Density-functional theory (DFT) model was employed to determine porous distribution. The mesopores volume was calculated as the difference between the amount of N_2 adsorbed at 0.95 ($V_{0.95}$) and the volume of micropores.

Raman spectroscopy was used to determine the grade of order and disorder in the materials. The test was carried out on FT-Raman dispersive spectrometer (model Bruker RFS/100) with a coupled microscope. It has a laser excitation source in the near-infrared (1064 nm, Nd_YAG). The moisture, volatile matter, fixed carbon, and ash contents were determined by proximate analysis.

The surface chemistry was determined through two characterization techniques. First, temperature-programmed decomposition (TPD) on a thermogravimetric analyzer (TG) coupled to a mass spectrophotometer, where the signals of CO and CO_2 were recorded. The experiments were programmed with a heating ramp of 10 °C/min up to 120 °C and another of 20 °C/min from 120 to 950 °C under a helium atmosphere. Second, X-ray photoelectron spectroscopy (XPS) carried out on VG-Microtech Mutilab 3000, equipped with a hemispherical electron analyzer with 9 channels (power of 2 to 200 Ev) and an X-ray radiation source with Mg and Al anodes, the radiation source was Mg-Kα (1253, 6 eV).

2.3. Electrochemical characterizations

2.3.1. Electrochemical tests in a three-electrode cell

The electrochemical characterization was performed at room temperature in a standard three-electrode cell system using a potentiostat (Biologic VMP-300) and H_2SO_4 (1 M) as electrolyte with a typical Ag/AgCl reference electrode and Pt wire as the counter electrode. The working electrode is a graphite sheet loaded with a homogeneous mixture of finely ground activated carbon synthesized and binder

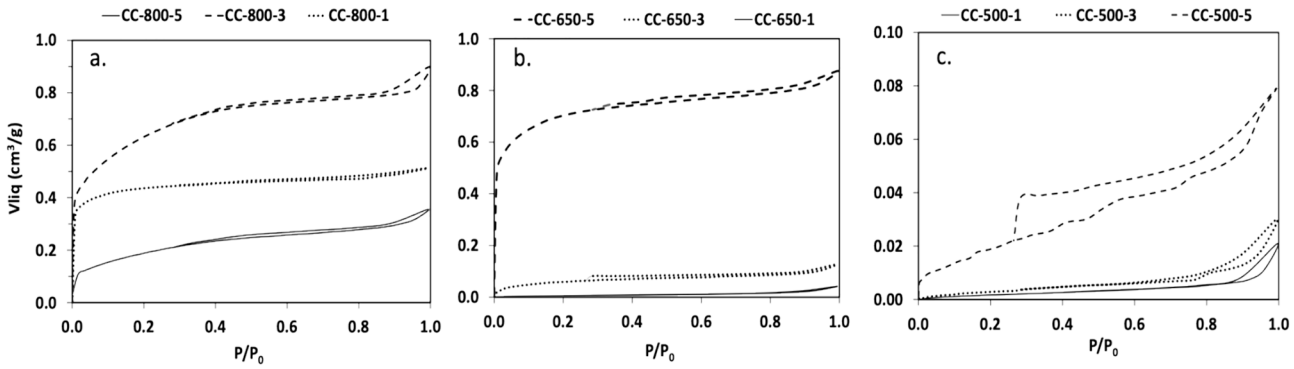

Fig. 1. N_2 adsorption–desorption isotherms at −196 °C of carbonized samples at different temperature. a) 800 °C; b) 650 °C and c) 500 °C.

(polytetrafluoroethylene, PTFE). The activated carbon-binder mixture was prepared mixing PTFE (60 % suspension in water) and activated carbon at a mass ratio of 90:10 (45 mg active carbon: 5 mg PTFE), and the paste was dried at 100 °C for 12 h. The pasted sample was deposited on a graphite sheet and impregnated with H_2SO_4 (1 M) for 48 h before being used for the electrochemical measurements, in order to ensure a better diffusion of the electrolyte ions in the pores of material.

Cyclic voltammograms (CV) tests were obtained at scan rates of 0.5, 5, 10, 20, and 30 mV/s within the range of −0.3 and 0.9 V (to avoid electrolysis of the water). The gravimetric capacitance C_{CV} (F/g) was calculated from CV curves by the following Eq. (1):

$$C_{CV} = \frac{\sum |I| \hat{A} \cdot \Delta t}{2m \hat{A} \cdot \Delta V} \quad (1)$$

Where $\sum |I| \Delta t$ is the area under the curve of current (A) vs time (s), m the mass of carbon material in the electrode (g), and ΔV the potential window (V).

Chronopotentiograms were carried out at a current loading between 125 and 2000 mA/g in a potential interval of −0.3 to 0.9 V. The gravimetric capacitance from these measurements C_{GD} (F/g), was calculated by the following Eq. (2):

$$C_{GD} = \frac{I_d \hat{A} \cdot \Delta t}{m \hat{A} \cdot \Delta V} \quad (2)$$

Where I_d is discharge current (A), Δt the discharge time (s), ΔV potential interval (V).

The electrochemical impedance spectroscopy (EIS) measurements were carried out from a frequency of 1 mHz to 100 kHz with a sinusoidal signal amplitude of 10 mV. The graphical analysis of these data was represented by means of Nyquist Plots.

2.3.2. Electrochemical tests in a two-electrode cell

The last electrochemical study was carried out in a two-electrode configuration. H_2SO_4 (1 M) and a glassy fibrous material were used as electrolyte and separator, respectively. The same procedure used in the three-electrode system was followed in the working electrode, only differing in the use of a graphite disk and in the amount of material deposited (5 mg of paste). Galvanotatic charge/discharge cycles was performed at different current densities (0.125 to 7 A/g) with a potential window of 0 to 1.2 V. Cycling/aging tests were carried out at 1 Ag^{-1} over 12,500 charge–discharge cycles. The gravimetric capacitance was calculated from chronopotentiograms following Eq. (3):

$$C_{GD} = \frac{I_d \hat{A} \cdot \Delta t}{m \hat{A} \cdot \Delta V} \hat{A} \cdot 4 \quad (3)$$

Where I_d is discharge current (A), Δt the discharge time (s), ΔV potential interval (V), and the factor 4 indicated the relation between the capacitance of the single electrode in a three-electrode system and the capacitance of the electrode in a two-electrode system.

Based on the galvanotactic charge/discharge data, specific energy $E\left(Wh\,kg^{-1}\right)$ and power density $P\left(W\,kg^{-1}\right)$ were calculated at different current densities using the Ragone plot. The Eqs. (4) and (5) were used:

$$E = \frac{C_{GD} \hat{A} \cdot \Delta V^2}{8 \hat{A} \cdot 3.6} \quad (4)$$

$$P = \frac{1}{2} \times \frac{I \hat{A} \cdot \Delta V}{m} \quad (5)$$

Where I is density current (A), ΔV potential interval (V), and m the mass of carbon material in the electrode (kg).

3. Results and discussion

3.1. Physicochemical characterization

3.1.1. Textural characterization

The nitrogen adsorption–desorption isotherms at −196 °C of samples synthesized from the cocoa husk are shown in Fig. 1, and three type of carbons can be distinguished: (i) CC-800-3, CC-650-5, CC-800-1 have type I-b isotherm, typical of wide microporous materials in accordance with IUPAC classification [44], (ii)CC-650-1, CC-500-5 y CC-500-3 have type II isotherm, indicating non-porous materials and (iii) CC-500-1, CC-

Table 1
Textural proprieties of materials.

Sample	SBET m^2/g	W_0 (N_2) cm^3/g	W_0 (CO_2) cm^3/g	L_0 nm (N_2)	L_0 nm (CO_2)	$V_{0.95}$ cm^3/g	Vmeso cm^3/g	Vmicro/Vtotal
CC-800-1	1032	0.46	0.15	1.71	1.57	0.50	0.05	0.91
CC-800-3	1444	0.79	0.12	2.97	1.81	0.90	0.18	0.88
CC-800-5	447	0.27	0.05	4.71	1.73	0.32	0.09	0.84
CC-650-1	16	0.01	0.08	2.94	1.23	0.03	0.02	0.19
CC-650-3	145	0.07	0.15	2.85	1.38	0.11	0.04	0.63
CC-650-5	1633	0.76	0.24	2.23	1.54	0.83	0.08	0.91
CC-500-1	53	0.00	0.05	4.18	1.37	0.01	0.01	0.19
CC-500-3	8	0.01	0.05	7.65	1.37	0.02	0.01	0.35
CC-500-5	5	0.03	0.10	5.12	1.47	0.07	0.04	0.43

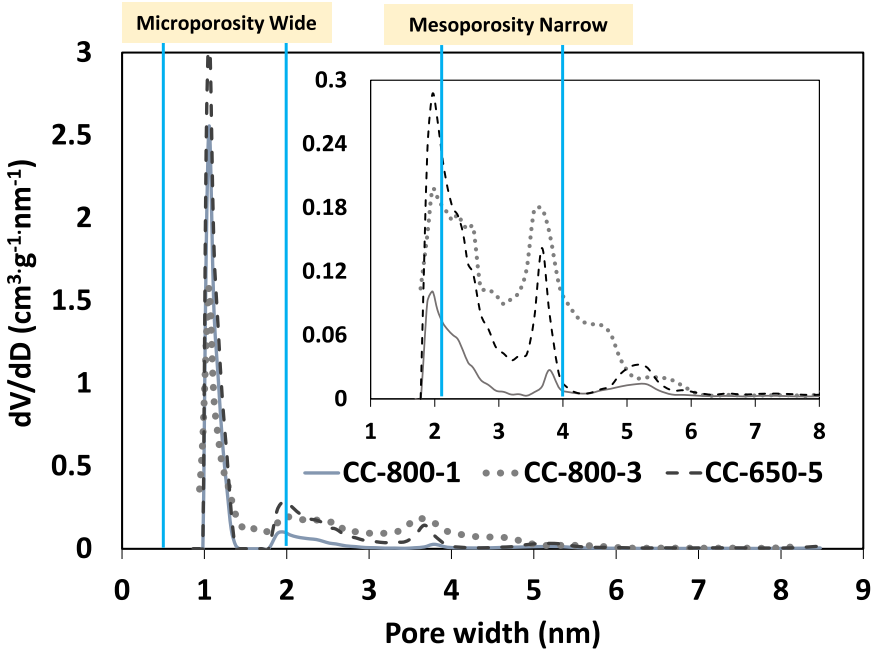

Fig. 2. Pore distribution of the CC-800-1, CC-650-5, CC-800-3 samples.

650-3, CC-800-5 samples have a hysteresis cycle (type IV-a) related to mesopores presence.

The isotherms shape displays some differences, in particular the width knee, which are related to micropore - mesopore structure. At relative pressures (P/P_0) about 0.01, sample CC-800-1 shows a sharp knee, and the plateau is nearly horizontal, indicating that the sample is primarily microporous with a narrow pore size distribution. On the contrary, both the knee and the slope of plateau in the CC-650-5 and CC-800-3 samples increase indicating that, in addition to microporosity, these samples may contain narrow mesopores.

Textural characterization with N_2 and CO_2 (Table 1) reveals an effect of the carbonization temperature and KOH ratio. At the lowest temperature, the samples show a lower BET surface area and absence of microporosity and mesoporous structure for all KOH ratios. When the temperature and KOH ratio increase, exits an effect in the modification of textural properties. However, high values of temperature and KOH ratio produce the destruction of microporosity and mesoporous structure. It manifests that the increase in the temperature and amount of KOH plays a more important role in the formation of microstructure. It is noting the importance of the effect between temperature and KOH ratio.

Some highlights show the influence of the activation parameters on the pore development of the material. The samples pyrolyzed at a lower temperature (500 °C) shows surface areas lower than 60 m^2/g, indicating that this temperature does not favor thermodynamically the reaction between the KOH and the cocoa husk. This phenomenon can be related to the change of free Gibbs energy, which is negative at temperatures higher than 570 °C [45]. Therefore, 500 °C is not enough to develop significant porosity in the materials (keeping in mind that the textural properties do not depend only on the activation parameters, but also on the raw material).

The KOH activation process generates activated carbon with a higher surface area. Among the prepared activated carbon, the maximum BET surface area was 1633 m^2/g, for the sample pyrolyzed at 650 °C, using the highest impregnation ratio (5:1), while at the other impregnation ratios the surface area was low.

Materials pyrolyzed at 800 °C indicated an increase in the surface area with a rise of the temperature for the impregnation ratios of 1:1 and 3:1 compared with the samples obtained at 650 °C; being the last impregnation ratio (3:1) the optimal at this temperature. Hence, material prepared with an impregnation ratio of 1:1 shown it is necessary for a major active agent proportion, however, when the impregnation ratio increased to 5:1, the microporosity of the material decreased indicating the collapse of porosity produced by the combination of a high impregnation ratio with an elevated pyrolysis temperature.

The data of CO_2 adsorption (Table 1) allow determining the micropore volume with narrow microporosity, with prose size smaller than 0.7 nm. The CC-800-1, CC-800-3, CC-800-5, and CC-650-5 samples present a $W_0(N_2) > W_0(CO_2)$, and therefore, these materials have a greater amount of micropores higher at 0.7 nm than narrow micropores, indicating the absence of N_2 diffusional restrictions and a high activation degree [46]. On the contrary, The CC-650-1, CC-650-3, CC-500-1, CC-500-3 and CC-500-5 samples developed narrower microporosity ($W_0(N_2) < W_0\ (CO_2)$), showing a low activation degree.

The narrow porosity probably cannot contribute to the formation of the double layer, since it restricts the access of electrolyte ions to the carbon surface. It is better to obtain a greater amount of micropores with diameters higher than 0.7 nm and a high surface area [47,48]. According to these criteria, the CC-800-1, CC-800-3 y CC-650-5 samples are selected to evaluate their electrochemical performance and deep analysis of their physical-chemical properties.

Fig. 2 shows the pore size distribution of the selected samples, and Table 1 shows the proportion of micropore volume with respect to the total pore volume. The CC-650-5, CC-800-1, and CC-800-3 carbonaceous materials have pores located principally in the microporosity range from 0.8 nm to 1.7 nm and micropores ratios (V_{micro}/V_{total}) of 0.91, 0.91, and 0.88 respectively. The CC-800-3 material has a higher amount of narrow mesoporosity than the materials CC-800-1 and CC-650-5. The microporosity presented in the samples are expected to allow the access of H^+ and SO_4^{-2} ions to the carbon surface, since the diameters of bare/solvated are 0.2/0.6 nm and 0.6/0.8 nm, [49] respectively. These physical characteristics allow ions adsorption in the electrolyte/electrode interface and the formation of the electrochemical double layer [50], while mesopores allow the diffusion of the electrolyte towards the micropores [51]. These characteristics in the pore size distribution can maximize the specific capacitance, which is very interesting for electrochemical applications.

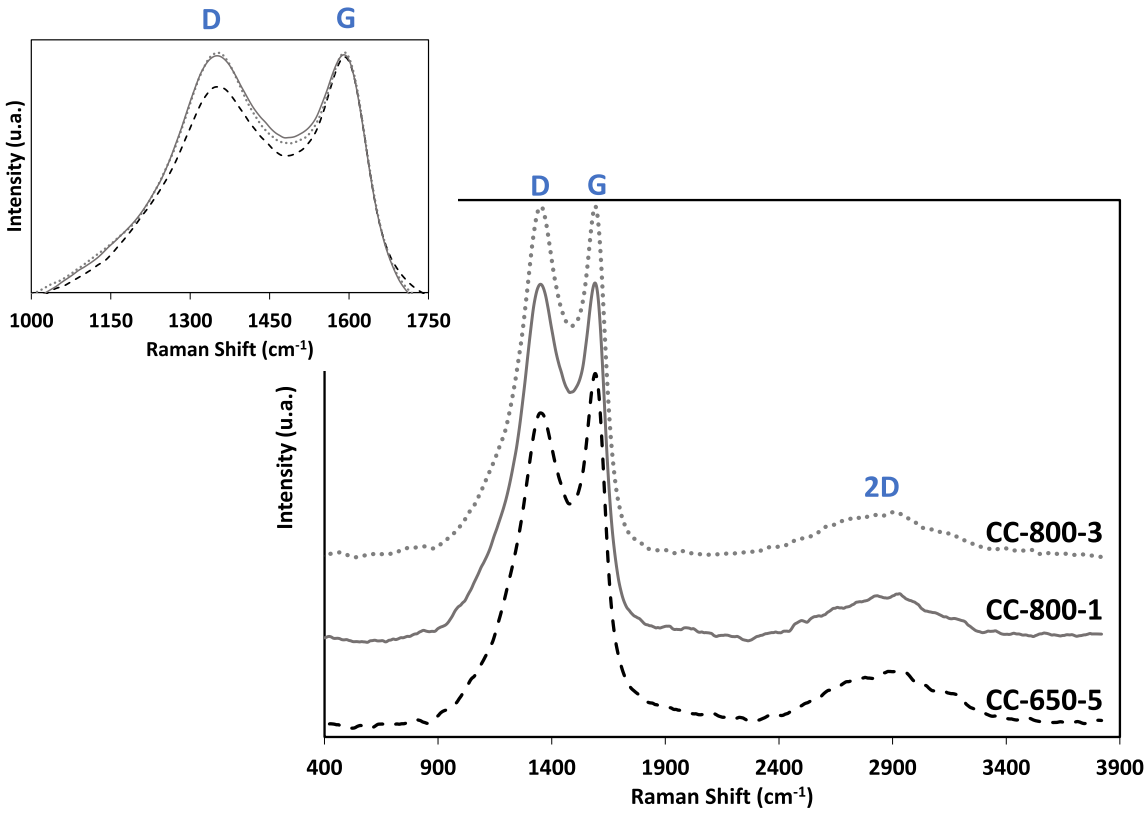

Fig. 3. Raman spectra of the porous carbons.

3.1.2. Raman spectroscopy

Raman spectra are presented in Fig. 3 for CC-800-1, CC-650-5 and CC-800-3 samples, showing two characteristic carbon bands. The first band, named D, oscillates between 1340 cm^{-1} to 1350 cm^{-1} and is related to the defects and disorder in the graphite structure of carbons. The second band, named G, is related to the stretching of the Sp^2 bond between carbons in graphite configuration, this band varies between 1590 cm^{-1} to 1601 cm^{-1}.

The intensity of the D band has the lowest value for the CC-650-5 material, and the increase of temperature to 800 °C increases the intensity in the C-800-1 and CC-800-3 samples, which could decrease the electrical conductivity in these materials with respect to sample CC-650-5 [52].

The ratio between the intensities of D band (I_D) with respect to G band (I_G) provides information about the degree of graphitization of the different carbons and the I_D/I_G values obtained for CC-800-1, CC-800-3, and CC-650-5 are 1.00, 0.98, and 0.88 respectively. These results suggest that the use of a lower temperature can promote higher crystallinity/graphitization during activation with KOH without significantly altering the carbon structural order as occurred in samples treated at higher temperatures.

In general, considering that activated carbons have high structural defects caused by the activation process [53], I_D/I_G was low within the values obtained for this type of material, in addition, a distinctive third peak corresponding to the 2D band characteristic of graphite is prominently present, indicating a high degree of graphitization in the samples [54]. These parameters indicate those materials with a higher degree of graphitization conduct better the electricity, which can be related with the intricate and inherent hierarchical structure of lignocellulosic materials like cocoa husk and the activation treatment with KOH.

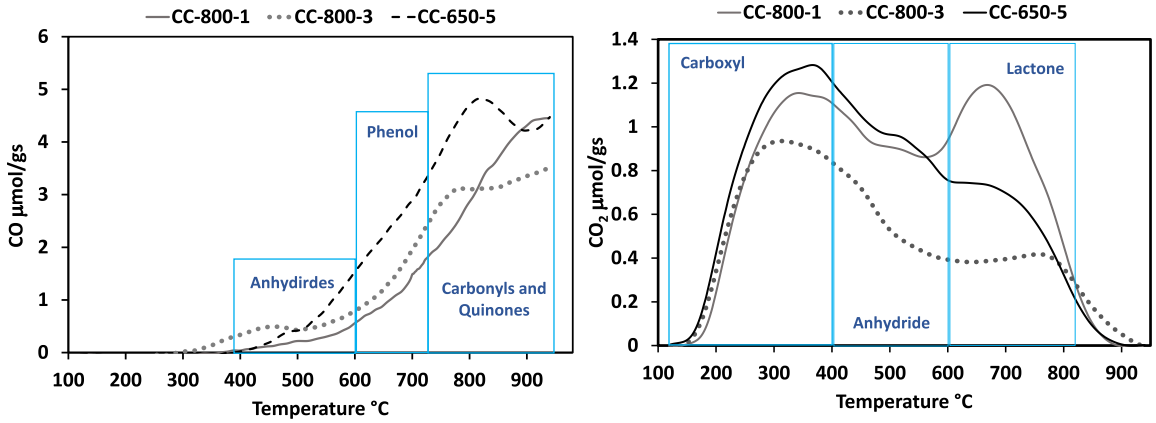

Fig. 4. TPD profiles: a) CO and b) CO_2.

Table 2
Surface chemistry of active carbons.

Sample	CO (μmol/g)	CO_2 (μmol/g)	O_{TPD} % wt	O_{XPS} % wt	CO/CO_2	O/C	Carbonyl, Quinone (μmol/g)	Phenol (μmol/g)	Carboxyl (μmol/g)	Lactone (μmol/g)	Anhydride (μmol/g)
CC-800-1	2716	1762	10.0	9.5	1.54	0.44	2316	359	130	1223	449
CC-800-3	2926	1153	8.4	9.0	2.54	0.08	2246	502	648	142	541
CC-650-5	4060	1679	11.9	12.1	2.42	0.14	2705	1325	651	279	779

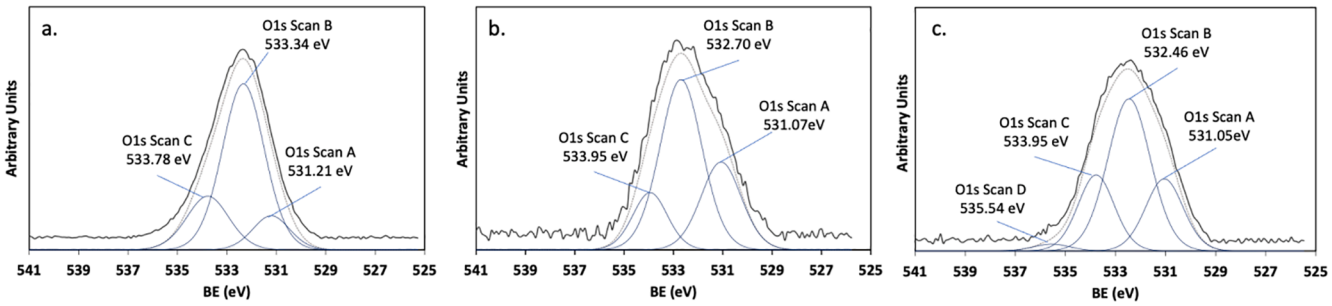

Fig. 5. O1s spectra of a) CC-800-1; b) CC-800-3 and c) CC-650-5.

3.1.3. Surface chemistry (TPD and XPS analysis

The surface functional groups of the samples was studied by temperature-programmed desorption coupled to mass spectrometry (TPD-Ms), since the surface oxygen groups decompose producing CO and CO_2 upon heating under inert gas in certain temperature ranges. Fig. 4 shows the CO and CO_2 profiles for samples CC-800-5, CC-800-3, and CC-650-5.

The CO profile (Fig. 4a) has a peak between 600 and 700 °C, attributed to phenolic groups decomposition, and the carbonyl, quinone and ether groups are decomposed at temperatures from 700 to 1000 °C. Small peaks around 400 to 600 °C K are also observed, corresponding to decomposition of anhydride compounds [55]. The CO_2 profile (Fig. 4b) has two main peaks, the first around 150 to 400 °C corresponding to carboxyl groups and the second around 650–725 °C matches with lactone groups. The CO and CO_2 profile were deconvoluted with PeakFit 4.12 software (see, Supplementary Material) and the results obtained allow quantitative comparison of the oxygenated groups. The results are summarized in Table 2.

CC-650-5 delivers the highest amount of CO during the decomposition, and this CO is principally associated with the presence of carbonyl and quinone groups (around 66 % of CO release) and phenolic groups (around 32 %). This outcome can be linked to the synthesis conditions of the materials, characterized by a substantial KOH proportion, promoting the formation of surface oxygenated groups. The use of a moderate carbonization temperature (650 °C) effectively prevented the decomposition of functional groups during the pyrolysis treatment, such as carbonyl, quinone, and phenolic groups. In contrast, the samples CC-800-1 and CC-800-3 exhibited lower proportions of groups associated with CO release, particularly in the case of phenolic groups being 13 % and 17 % respectively. This decrease can be attributed to the utilization of higher pyrolysis temperature, which partially decompose these groups.

CC-800-1 exhibited the highest CO_2 release, mainly by the contribution of the lactone functional groups (around 69 %), and carboxyl groups (around 39 %) are the main contribution for CC-650-5. The high content of O on these samples can explain the decrease in BET surface area, that is, CC-800-1 and CC-650-5 show a decrease in micro-mesopores structure, and a major concentration of groups related to CO_2 release compared with CC-800-1 sample. This trend can be also observed in the CO/CO_2 ratio, which is lower for CC-800-1 than for samples CC-800-3 and CC-650-5 since the amount of CO_2-evolving groups, such as lactones, is greater in this sample [56].

The surface composition of samples was analyzed by XPS (Fig. 5), which provided information regarding the electronic states and chemical environment of carbon (C) and oxygen (O) surface atoms. The surface percentage of oxygen and O/C ratio obtained from XPS are displayed in Table 2. The CC-800-1 sample shows the highest amount of oxygen, followed CC-650-5 and CC-800-3 sample, and these values are in accordance with TPD data.

The O1s spectra (Fig. 5) allow identifying the type of bonds in the oxygenated functional groups, and three representative peaks are observed in the deconvolution. The peak at 531.0–531.8 eV is related to C═O bonds, the peak at 532.3 eV represents C—O bonds, and the peak at 533.8 eV corresponds to C-OH bond [55,36]. Each type of bond

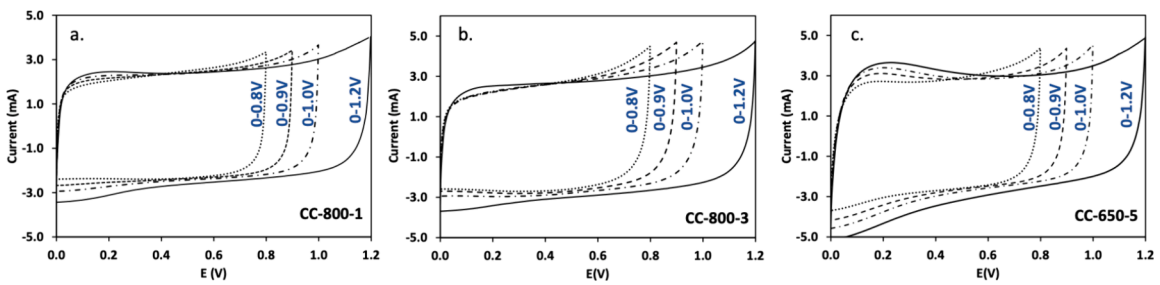

Fig. 6. Exploration of the operating windows in aqueous electrolyte (1 M H_2SO_4) in a two-electrode system: a) CC-800-1; b) CC-800–3; c) CC-650-5.

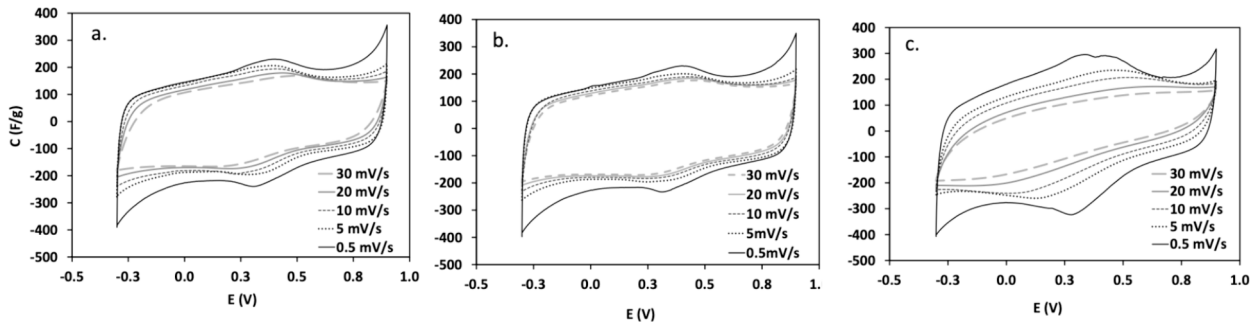

Fig. 7. Cyclic voltammograms of activated carbons using a three-electrode cell in 1 M H_2SO_4 at different scan rate: (a) CC-800-1, (b) CC-800-3, (c) CC-650-5.

Table 3
Capacitances contribution from voltammograms at 0.5 mV/s using a three-electrode cell in 1 M H_2SO_4.

Sample	Cvc (F/g)	Cdl (F/g)	Cps (F/g)
CC-800-1	191	186	5
CC-800-3	207	195	12
CC-650-5	222	192	30

identified in the spectra can be related to oxygenated functional group. The C═O bond is present in groups such as carboxyls, lactones carbonyls, anhydrides, and quinones, while C—O and C-OH bonds come from carboxyl groups and phenols. The results of the obtained bonds coincide with the oxygenated functional groups identified by TPD characterization.

An appropriate level of oxygenated functional groups on the carbon surface is important because provides polarity and improves interaction with the aqueous electrolytes. Carbons with low oxygen content are hydrophilic, hindering the wettability of the electrode, while an excess of oxygen could cause resistance of electrolyte ions, affecting in both cases the electrochemical performance [57,58]. In addition, some oxygenated groups can improve the capacitance of the electrode since they favor the pseudocapacitance, which allows the redox reactions to occur and favor a greater energy storage [32].

3.2. Electrochemical characterization

3.2.1. Cyclic voltammetry (CV)

The electrochemical performance was evaluated by means of CV using H_2SO_4 1 M as electrolyte. The CVs were obtained for two and three electrode systems. The two-electrode configuration allowed determining the optimal potential window to evaluate the electrochemical capacity of the symmetrical supercapacitor device. In Fig. 6 is displayed the results at a scan rate of 5mv/s for different operating windows. The maximum value is limited to 1.2 V to avoid the decomposition of water, a common phenomenon in aqueous electrolytes, which starts at around 1.23 V [59]. The voltammograms remain stable at voltages near 1.23 V.

One reason for this behavior could be that the materials employed are not selective to the reduction or oxidation reactions of water. This is consistent with findings of Lin and et al [60], who tested the same potential window (0 to 1.2 V) and employed 0.5 M H_2SO_4 aqueous electrolyte, and did not observe the generation of hydrogen nor oxygen products. This window was chosen for assessments of the symmetric supercapacitor device (two - electrode system).

Fig. 7 depicts cyclic voltagrams (CV) of all the samples at different rates between 0.5 and 30 mV/s using a three-electrode system and 1 M H_2SO_4 as electrolyte. The three samples show cuasi-rectangular voltagrams indicating the contribution of the electrical double layer. The faradic peaks are identified in a potential range between 0.2 to 0.4 V (vs Ag/AgCl), which related to the pseudofaradic redox reactions of the oxygenated functional groups that contributed to the pseudocapacitance.

CC-800-1 and CC-800-3 samples exhibited similar voltagrams whereas CC-650-5 sample displayed noticeable differences in CV curve shape. This behavior is due to these pseudo-faradic peaks, that produces a higher capacitance (Table 3). Nevertheless, as the scan rate increased, the CC-650-5 voltammograms lose their shape, showing more pronounced diffusion problems compared to CC-800-3 and CC-800-5 samples, which maintain their shape even at scan rates of up to 30 mV/s.

The capacitance of the materials prepared can be understood by two contribution, electrical double layer and pseudo-faradic contribution. These phenomena were quantified and the store capacity (Cdl), pseudofaradic contribution (Cps) and total capacitance (Cvc) values were calculated and compiled in Table 3. It is assumed that, in the cyclic voltammograms, the electrical double layer manifests itself as a rectangular shape, which allows to determine the storage capacity in this region, Cdl. Deviations from this rectangular shape, such as the peaks illustrated in Fig. 8, are due to pseudofaradic contribution, Cps.

The CC-650-5 sample exhibits a more substantial pseudocardiac contribution (see, Fig. 8), and this phenomenon could be attributed to the elevated oxygen content present on the surface of the material, as revealed by the TPD and XPS results. The oxygen presence facilitates Faradic reactions leading to more pronounced oxidation–reduction peaks in comparison to the CC-800-1 and CC-800-3 samples, which possess less oxygen groups.

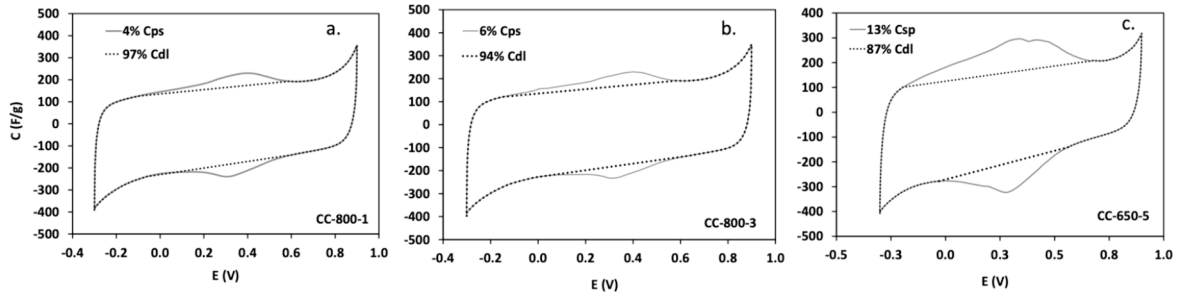

Fig. 8. Pseudofaradic and electrical double layer contributions (VCs at 0.5 mV/s) in 1 M aqueous H_2SO_4 using a three electrode system.

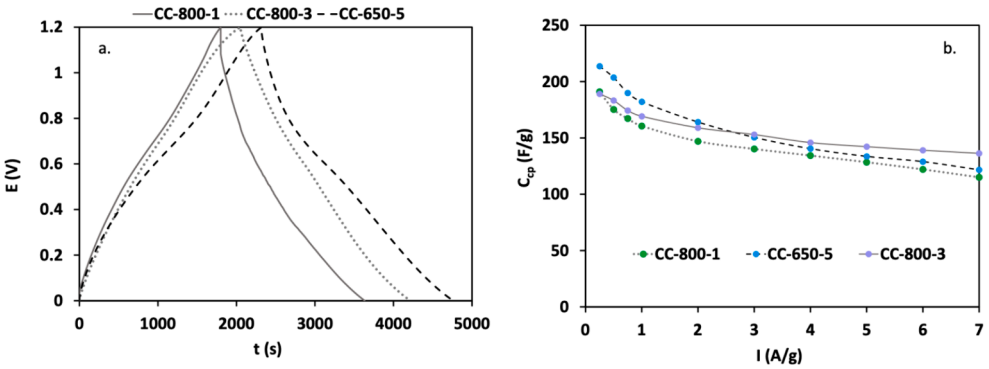

Fig. 9. Chronopotentiograms of activated carbons using a three-electrode cell in 1 M H_2SO_4 at 125 mA/g. Influence of current loading on C_{GD} gravimetric capacitance of activated carbons.

Table 4
Electrochemical performance: Gravimetric capacitance from chronopotentiograms (C_{GD}) and resistance to charge transfer (R_{CT}), internal resistance (R_Σ) from EIS.

Sample	Ccp (F/g) at 125 mA/g	Ccp (F/g) at 1 A/g	Ccp (F/g) at 7A/g	$\%C_{cp}$ retention	R_{CT} (Ω)	R_Σ (Ω)
CC-800-1	211	161	115	60	2.6	1.3
CC-800-3	226	169	136	72	1.13	1.28
CC-650-5	258	182	122	57	0.31	2.45

3.2.2. Galvanostatic charge–discharge (GCD)

The chronoamperometries results are plotted in Fig. 9a, at a current density of 125 mA g^{-1}. It is observed that they have quasi-triangular shapes and are nonlinear in the charge–discharge zone, indicating typical double layer and pseudocapacitive behavior. Capacitances were calculated for different current densities from 125 mA g^{-1} to 7 A g^{-1} (Table 4) and their variations were plotted with respect to current density in Fig. 9b. For the three samples, it is observed that the capacitance decreases as the current density increases, and this behavior is expected since at high current intensities the formation of the electrical double layer becomes more difficult. The CC-650-5 retention capacity is lowest, despite having high capacitance at the beginning.

This behavior may be associated with its structure and surface chemistry, which is consistent with the results observed in the CV curves. These results again suggest the discussion of two important points: *i)* the contribution of the double layer in the specific capacitance, considering that depends exclusively on the surface area, volume, and distribution of the micro-mesopores of the materials, *ii)* the influence of the redox reactions on the capacitance, which depend on the surface groups present.

3.2.3. Relationship between electrochemical performance and structural properties

It is known that supercapacitors are devices that can store energy through the adsorption of charge that accumulates electrostatically, a mechanism called electrical double layer. Therefore, the surface specify area is crucial for charge adsorption [61]. At low current density, the materials used as electrodes show a direct relationship between the surface area and the capacitance, however, when current density increases this tendency changes. This behavior is related to pore

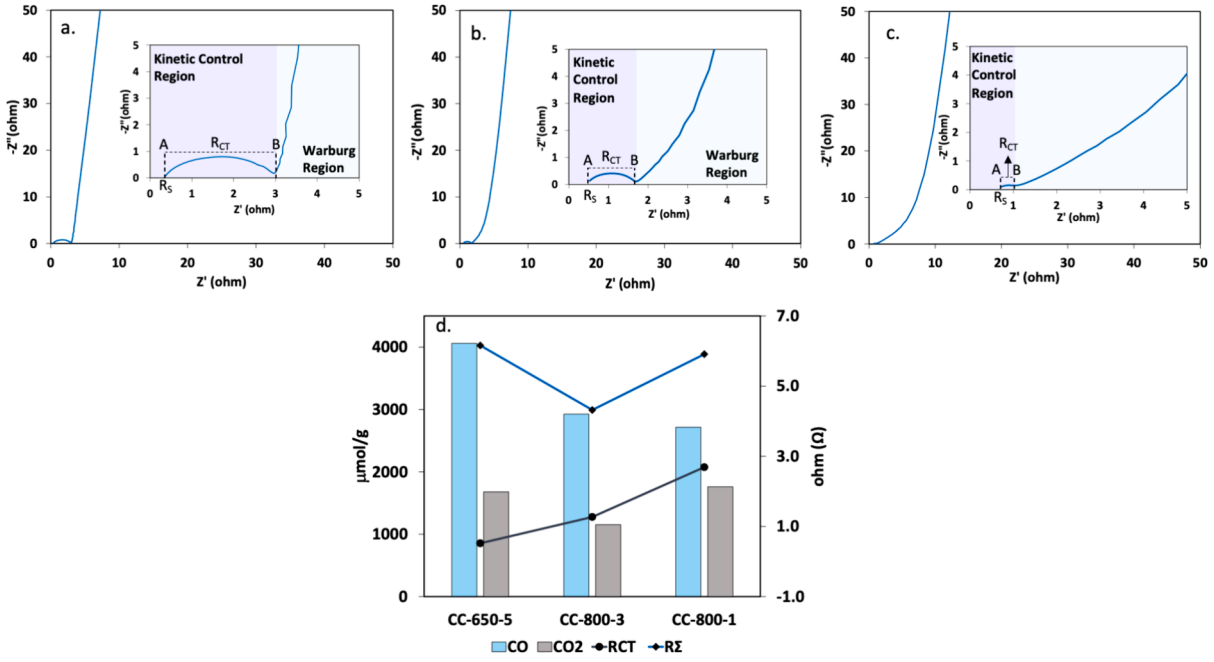

Fig. 10. Nyquist plot: a) CC-800-1, b) CC-800-3, c) CC-650-5, and d) variation of the R_Σ and R_{CT} with total CO and CO_2 content.

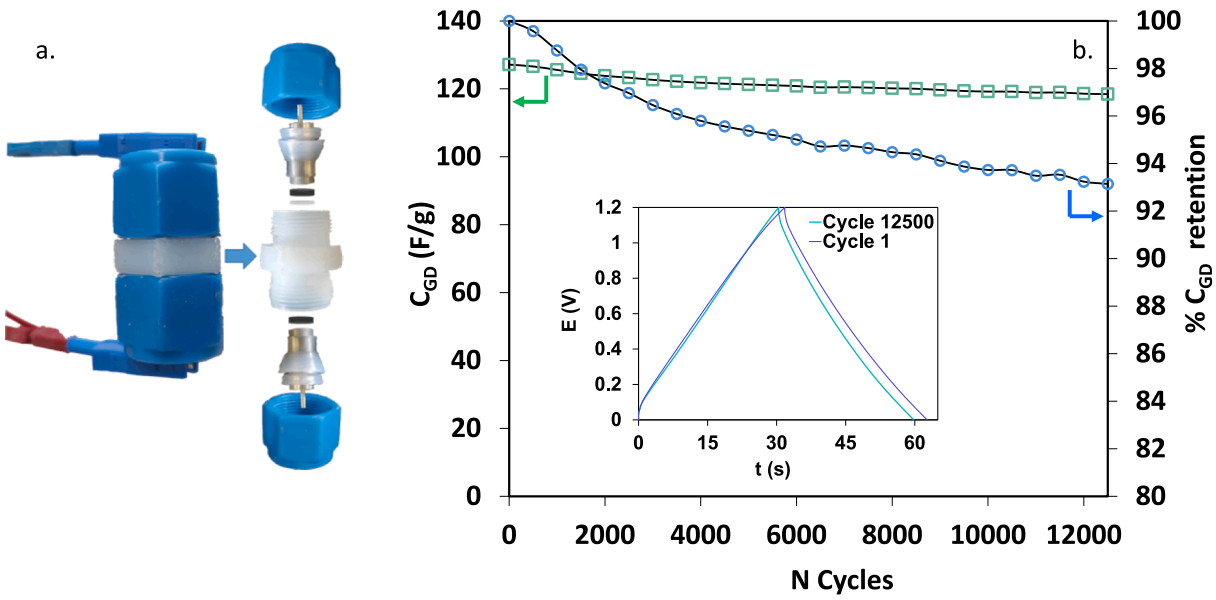

Fig. 11. a) Configuration of a two-electrode system and, b) variation of capacitance and holding capacity with the number of charge and discharge cycles for cc-800-3 sample using 1 M H_2SO_4 as electrolyte.

distribution since the high surface area is not the only factor to guarantee good electrochemical performance. In the case of the CC-800-3 sample, it was previously identified that, in addition to have microporosity, it also has a greater amount of mesoporosity, which reduces the diffusion problems of the electrolyte ions serving as channels for the rapid transport to micropores. This explains why, at high current densities, this sample specifically obtained a higher retention capacity [54,62]. The CC-650-5 sample shows a lower retention capacity due to its limited mesoporosity, being difficult for the electrolyte to reach micropores.

3.2.4. Relationship between electrochemical performance and surface oxygenated groups

Surface oxygenated functional groups can play two important roles in the electrochemical performance of materials. First, they increase polarity, thus improving the interaction of the carbon materials with aqueous electrolytes. Second, their contribution increases in overall capacitance through redox reactions that promote pseudocapacitance [63]. However, not all oxygenated functional groups contribute to the improvement of the electrochemical response. Previous studies have reported that the functional groups related to CO release in thermal decomposition improve the capacitance of the electrode [64], since the quinone, carbonyl and phenol groups, have bonds such as C-OH and C═O, which allow good wettability of carbonaceous materials and also promote the pseudocapacity due to these types of bonds are involved in electron transfer reactions [65]. Therefore, by applying a voltage for charging and discharging the electrodes, these groups provide better stability. On the contrary, the functional groups related to CO_2 release do not allow the delocalization of electrons, since they have a strong electron-withdrawing nature, thus reducing the electrical conductivity and the capacitance [66].

As previously observed, the CC-650-5 sample obtained a greater amount of functional groups related to CO release, allowing the improvement in the wettability of the material with the electrolyte. This behaviour was verified by the electrochemical impedance spectroscopy (EIS), which allow to study the kinetic and diffusional behavior of ions at the electrode/electrolyte interface. The results are represented in a Nyquist plot (Fig. 10a-c). This representation can be divided into two regions. At low and medium frequencies correspond to the kinetic control region and high to Warburg region.

In the kinetic control region, point A denotes the system resistance (R_S), which includes the collective resistances between the electrolyte, working electrode, and current collector [67]. The semicircle stretching from point A to point B displays the resistance to electron transfer (R_{CT}). In the Warburg region, showcases control and mass transfer. The non-vertical line in this area is related to the formation of the electric double layer. Their slopes can suggest if the charging process was directed by the electric double layer formation (slope greater than 45°) or limited by ion diffusion (slope less than 45°) [68,69].

Fig. 10d shows that CC-650-5 sample has the lowest resistance to electron transfer (R_{CT}), indicating that the significant presence of CO-related functional groups, such as quinones and carbonyl groups, which are active at acidic pH [70] and can promote electron transfer and reduce resistance. CC-800-3 and CC-800-1 samples contain fewer of these functional groups. CC-800-1 sample has a significantly higher R_{CT} resistance, which may be due to its higher content of oxygenated functional groups associated with CO_2. As a result, electron transfer becomes less effective, leading to lower electrical conductivity and, in turn, increased R_{CT}. In summary, the hierarchy of R_{CT} resistance is as follows: CC-800-1 > CC-800-3 > CC-650-5.

The calculation of internal resistance (R_Σ) was performed to measure the impedance against the movement of ions and electrons within the electrode structure (see, Table 4). CC-650-5 sample exhibits higher resistance R_Σ compared to the other two samples, although having a lower R_{CT} due to its high content of CO groups. This could be due to its significant microporosity with limited mesoporosity, which limits the transport of electrolyte ions through the electrode pores. This is evidenced by the small slope of the non-vertical line in the Warburg zone of the Nyquist plot (Fig. 10a-b), indicating diffusion process. CC-800-3 and CC-800-3 samples show non-vertical lines in the Warburg zone with slopes exceeding 45 °C. This suggests that the charging process was dominated by the formation of the electrical double layer [1].

The CC-800-3 sample exhibited superior electrochemical performance in comparison to the other samples, which can be attributed to several key factors: *i)* an optimal microporosity, ensuring a substantial surface area available for ion adsorption which lead to higher capacitance, *ii)* effective mesoporosity, facilitating the efficient transport of the electrolyte into micropores. This attribute translated into superior charge-holding capacity, particularly at high current densities and, *iii)* a favorable balance of oxygenated CO-related surface groups while maintaining lower levels of CO_2-related groups. This unique surface chemistry improved the material wettability, reducing charge resistance

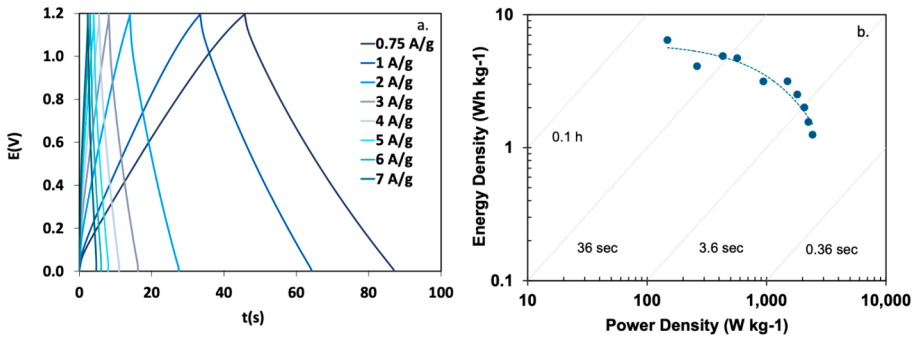

Fig. 12. a) Galvanostatic charge/discharge of activated carbons using a two-electrode cell in 1 M H_2SO_4 at different current densities. b) Ragone plot.

and promoting redox reactions, thereby contributing to pseudocapacitance.

Due to these remarkable characteristics, the CC-800-3 sample emerged as the preferred electrode for assessing its electrochemical performance within a two-electrode system, as depicted in Fig. 11a. The stability of this sample was subjected to rigorous testing, including an exhaustive 12,000 cycles of charge–discharge at 1A/g. The sample demonstrated exceptional stability throughout the entire duration of the test, displaying a capacitance retention rate of 93 % even after the demanding 12,000 cycles as is illustrated in Fig. 11b.

It can be observed in Fig. 12a that the galvanostatic charge/discharge curves maintained a consistent shape, even when subjected to high current densities. These results underscore the reliability and suitability of materials prepared for demanding applications. In Fig. 12b, a comprehensive overview of its performance using a Ragone plot. It can be observed an energy density of 6.43 Wh/Kg at a power density of 148 W/kg for the CC-800-3 sample in the two-electrode system.

4. Conclusions

The textural and chemical properties of activated carbons derived from cocoa husk are influenced by synthesis conditions such as temperature and the ratio of potassium hydroxide (KOH). It is established that the activated carbons synthesized under optimum conditions (temperature and alkali ratio) are mainly microporous materials with high surface area and pore volumes. The electrochemical performance of activated carbons used as electrodes was found to be related to their textural and chemical characteristics. It was crucial to have a combination of micro- and mesopores in the material to improve both capacitance and holding capacity at high current densities.

The presence of oxygen significantly affected the electrochemical properties. CO-related functional groups demonstrated a beneficial impact in reducing electron passage resistance, which enhanced the pseudofaradaic contribution. Conversely, CO_2-related functional groups amplified the resistance, compromising the electrode performance. The sample carbonized at 800 °C and impregnated with a 3:1 ratio shows the best chemical and textural properties. The best performance corresponds to the CC-800-3 sample with a lower resistance to charge transfer and a high capacitance attributed by the double electric layer and redox reactions that gave rise to the pseudocapacitance.

CRediT authorship contribution statement

Lilian D. Ramírez-Valencia: Writing – original draft, Software, Methodology, Investigation, Formal analysis, Data curation. **Franz E. López-Suárez:** Writing – review & editing, Validation, Supervision, Resources, Project administration, Methodology, Investigation, Funding acquisition, Formal analysis, Conceptualization. **Laura R. Conde:** Validation, Resources, Methodology, Funding acquisition, Conceptualization. **Esther. Bailón-García:** Validation, Resources, Methodology. **Agustín Bueno-López:** Writing – review & editing, Validation, Funding acquisition. **Agustín F. Perez-Cadenas:** Validation, Resources, Funding acquisition.

Declaration of competing interest

The authors declare that they have no known competing financial interests or personal relationships that could have appeared to influence the work reported in this paper.

Acknowledgments

Franz E. López – Suárez is supported by a Maria Zambrano (PRTR-C17.I1, ZAMBRANO 2114) postdoctoral fellowship from the University of Alicante and the Spanish Ministry of Universities, funded by the European Union-Next-GenerationEU/PRTR (Plan de Recuperación, Transformación y Resiliencia) and Generalitat Valenciana (Projects CIPROM/2021/74, MFA/2022/036). Lilian D. Ramírez-Valencia is grateful to the Colombian Ministry of Sciences, Technology and Innovation (MINCIENCIAS) for supporting her PhD studies (860). To María M. Molina and Leidy G. Ibagón for their contribution to the samples obtention.

Appendix A. Supplementary data

Supplementary data to this article can be found online at https://doi.org/10.1016/j.jelechem.2024.118325.

References

[1] S. Ould Amrouche, D. Rekioua, T. Rekioua, S. Bacha, Overview of energy storage in renewable energy systems, *Int. J. Hydrogen Energy*, 41(45) (2016) 20914–20927, doi: 10.1016/j.ijhydene.2016.06.243.
[2] A.N. Abdalla, et al., Integration of energy storage system and renewable energy sources based on artificial intelligence: An overview, J Energy Storage 40 (2021), https://doi.org/10.1016/j.est.2021.102811.
[3] A. A. Kebede, T. Kalogiannis, J. Van Mierlo, M. Berecibar, A comprehensive review of stationary energy storage devices for large scale renewable energy sources grid integration, *Renew. Sustain. Energy Rev.*, 159 (2022). 10.1016/j.rser.2022.112213.
[4] Y.A. Maletin, N.G. Stryzhakova, S.O. Zelinskyi, S.I. Chernukhin, Energy storage technologies based on electrochemical double layer capacitors: A review, Theor. Exper. Chem. 57 (5) (2021) 311–324, https://doi.org/10.1007/s11237-021-09700-7.
[5] Z. S. Iro, C. Subramani, S. S. Dash, A brief review on electrode materials for supercapacitor, *International Journal of Electrochemical Science*, vol. 11, no. 12. Electrochemical Science Group, (2016) pp. 10628–10643. 10.20964/2016.12.50.
[6] M. E. Şahin, F. Blaabjerg, A. Sangwongwanich, A comprehensive review on supercapacitor applications and developments, *Energies*, 15(3) (2022). 10.3390/en15030674.
[7] R. Kumar *et al.*, An overview of recent progress in nanostructured carbon-based supercapacitor electrodes: From zero to bi-dimensional materials, *Carbon*, 193 (2022) 298–338. 10.1016/j.carbon.2022.03.023.
[8] Y. Zhang, C. Li, F. Cao, A. Noori, M. F. Mousavi, X. Xia, Carbon in electrochemical energy, *Mater. Res. Bull.*, 152 (2022). 10.1016/j.materresbull.2022.111852.
[9] S. Najib, E. Erdem, Current progress achieved in novel materials for supercapacitor electrodes: Mini review, *Nanoscale Adv.* Royal Society of Chemistry, 1(8) (2019), 2817–2827. 10.1039/c9na00345b.

[10] P. Simon, Y. Gogotsi, Capacitive energy storage in nanostructured carbon-electrolyte systems, Acc. Chem. Res. 46 (5) (2013) 1094–1103, https://doi.org/10.1021/ar200306b.

[11] H. Wang, et al., Highly compressible supercapacitor based on carbon nanotubes-reinforced sponge electrode, J. Alloys Compd. 786 (2019) 995–1004, https://doi.org/10.1016/j.jallcom.2019.01.303.

[12] X. Wu, et al., Aqueous-based, high-density nanoporous carbon xerogels with high specific surface area for supercapacitors, J. Porous Mater. 29 (1) (2022) 87–95, https://doi.org/10.1007/s10934-021-01149-2.

[13] C. (John) Zhang, V. Nicolosi, Graphene and MXene-based transparent conductive electrodes and supercapacitors, *Energy Storage Mater.*, 16 (2019) 102–125. 10.1016/j.ensm.2018.05.003.

[14] A. S. Lemine, M. M. Zagho, T. M. Altahtamouni, N. Bensalah, Graphene a promising electrode material for supercapacitors—A review, *Int. J. Energy Res.*, 42(14) (2018) 4284–4300. 10.1002/er.4170.

[15] S. Thomas, A. B. Gueye, R. K. Gupta, Eds., *Nanostructured materials for supercapacitors*, in: Advances in Material Research and Technology. Cham: Springer International Publishing, 2022. 10.1007/978-3-030-99302-3.

[16] A. G. Olabi, Q. Abbas, A. al Makky, M.A. Abdelkareem, Supercapacitors as next generation energy storage devices: Properties and applications, *Energy*, 248 (2022), 10.1016/j.energy.2022.123617.

[17] J. Panak Balentić et al., Cocoa shell: A by-product with great potential for wide application, *Molecules (Basel, Switzerland)*, 23(6) (2018). 10.3390/molecules23061404.

[18] D.C.G. Okiyama, S.L.B. Navarro, C.E.C. Rodrigues, Cocoa shell and its compounds: Applications in the food industry, *Trends Food Sci. Technol.*, 63 (2017) 103–112. 10.1016/j.tifs.2017.03.007.

[19] International cocoa organization, Quarterly Bulletin of Cocoa Statistics, *Vol. XLVIII, No.3* (2022).

[20] F. Ahmad, W.M.A.W. Daud, M.A. Ahmad, R. Radzi, The effects of acid leaching on porosity and surface functional groups of cocoa (Theobroma cacao)-shell based activated carbon, Chem. Eng. Res. Des. 91 (6) (2013) 1028–1038, https://doi.org/10.1016/j.cherd.2013.01.003.

[21] P. Manasa, S. Sambasivam, F. Ran, Recent progress on biomass waste derived activated carbon electrode materials for supercapacitors applications—A review," *J. Energy Stor.*, 54(2022). 10.1016/j.est.2022.105290.

[22] L. Miao, Z. Song, D. Zhu, L. Li, L. Gan, M. Liu, Recent advances in carbon-based supercapacitors, *Mater. Adv.*, 1(5) (2020) 945–966. 10.1039/d0ma00384k.

[23] Suhdi, S.C. Wang, Fine activated carbon from rubber fruit shell prepared by using $ZnCl_2$ and koh activation, *Appl. Sci. (Switzerland)*, 11(9) (2021), 10.3390/app11093994.

[24] H.K. Yağmur, İ. Kaya, Synthesis and characterization of magnetic $ZnCl_2$-activated carbon produced from coconut shell for the adsorption of methylene blue, J. Mol. Struct. 1232 (2021), https://doi.org/10.1016/j.molstruc.2021.130071.

[25] F. Mbarki, T. Selmi, A. Kesraoui, M. Seffen, Low-cost activated carbon preparation from Corn stigmata fibers chemically activated using H_3PO_4, $ZnCl_2$ and KOH: Study of methylene blue adsorption, stochastic isotherm and fractal kinetic, Ind. Crop. Prod. 178 (2022), https://doi.org/10.1016/j.indcrop.2022.114546.

[26] A.H. Jawad, A. Saud Abdulhameed, L.D. Wilson, S.S.A. Syed-Hassan, Z.A. ALOthman, M. Rizwan Khan, High surface area and mesoporous activated carbon from KOH-activated dragon fruit peels for methylene blue dye adsorption: Optimization and mechanism study, *Chinese J. Chem. Eng.*, 32 (2021) 281–290. 10.1016/j.cjche.2020.09.070.

[27] S. Shi, Y. Liu, Nitrogen-doped activated carbons derived from microalgae pyrolysis by-products by microwave/KOH activation for CO_2 adsorption, Fuel 306 (2021), https://doi.org/10.1016/j.fuel.2021.121762.

[28] I. Syafiqah Ismail, N. Adilla Rashidi, S. Yusup, Production and characterization of bamboo-based activated carbon through single-step H_3PO_4 activation for CO_2 capture, Pollut. Prev. Sustain. 10.1007/s11356-021-15030-x/Published.

[29] O. Bag, K. Tekin, S. Karagoz, Microporous activated carbons from lignocellulosic biomass by KOH activation, Fullerenes Nanotubes Carbon Nanostruct. 28 (12) (2020) 1030–1037, https://doi.org/10.1080/1536383X.2020.1794850.

[30] X. Li, et al., Preparation of capacitor's electrode from sunflower seed shell, Bioresour. Technol. 102 (2) (2011) 1118–1123, https://doi.org/10.1016/j.biortech.2010.08.110.

[31] D. Liu, W. Zhang, H. Lin, Y. Li, H. Lu, Y. Wang, A green technology for the preparation of high capacitance rice husk-based activated carbon, J. Clean. Prod. 112 (2016) 1190–1198, https://doi.org/10.1016/j.jclepro.2015.07.005.

[32] K. Wang, et al., Promising biomass-based activated carbons derived from willow catkins for high performance supercapacitors, Electrochim. Acta 166 (2015) 1–11, https://doi.org/10.1016/j.electacta.2015.03.048.

[33] L. Yin, Y. Chen, D. Li, X. Zhao, B. Hou, B. Cao, 3-Dimensional hierarchical porous activated carbon derived from coconut fibers with high-rate performance for symmetric supercapacitors, Mater. Des. 111 (2016) 44–50, https://doi.org/10.1016/j.matdes.2016.08.070.

[34] P. Hepsiba, S. Rajkumar, E. Elanthamilan, S.F. Wang, J. Princy Merlin, Biomass-derived porous activated carbon from anacardium occidentale shell as electrode material for supercapacitors, New J. Chem. (2022), https://doi.org/10.1039/d2nj01041k.

[35] V. Thirumal, et al., Characterization of activated biomass carbon from tea leaf for supercapacitor applications, Chemosphere 291 (2022), https://doi.org/10.1016/j.chemosphere.2021.132931.

[36] A. Elmouwahidi, E. Bailón-García, A.F. Pérez-Cadenas, F.J. Maldonado-Hódar, F. Carrasco-Marín, Activated carbons from KOH and H_3PO_4-activation of olive residues and its application as supercapacitor electrodes, Electrochim. Acta 229 (2017) 219–228, https://doi.org/10.1016/j.electacta.2017.01.152.

[37] R. Chen, et al., Preparation and characterization of activated carbons from tobacco stem by chemical activation, J. Air Waste Manag. Assoc. 67 (6) (2017) 713–724, https://doi.org/10.1080/10962247.2017.1280560.

[38] E.M. Mistar, T. Alfatah, M.D. Supardan, Synthesis and characterization of activated carbon from Bambusa vulgaris striata using two-step KOH activation, J. Mater. Res. Technol. 9 (3) (2020) 6278–6286, https://doi.org/10.1016/j.jmrt.2020.03.041.

[39] N. Karakehya, Effects of one-step and two-step KOH activation method on the properties and supercapacitor performance of highly porous activated carbons prepared from Lycopodium clavatum spores, Diam. Relat. Mater. 135 (2023) 109873, https://doi.org/10.1016/j.diamond.2023.109873.

[40] Y. Jiang, et al., Facile method to produce sub-1 nm pore-rich carbon from biomass wastes for high performance supercapacitors, J. Colloid Interface Sci. 612 (2022) 213–222, https://doi.org/10.1016/j.jcis.2021.12.144.

[41] T. Zhang, M. Zheng, N. Li, H. Lu, S. Zhang, J. Cao, Macro-microporous carbon for supercapacitors derived from rape seed shell, Mater. Lett. 105 (2013) 43–46, https://doi.org/10.1016/j.matlet.2013.04.055.

[42] H. Yang, Y. Tang, X. Huang, L. Wang, Q. Zhang, Activated porous carbon derived from walnut shells with promising material properties for supercapacitors, J. Mater. Sci. Mater. Electron. 28 (24) (2017) 18637–18645, https://doi.org/10.1007/s10854-017-7813-6.

[43] D.C. Martínez-Casillas, et al., A sustainable approach to produce activated carbons from pecan nutshell waste for environmentally friendly supercapacitors, Carbon N Y 148 (2019) 403–412, https://doi.org/10.1016/j.carbon.2019.04.017.

[44] M. Thommes, et al., Physisorption of gases, with special reference to the evaluation of surface area and pore size distribution (IUPAC Technical Report), Pure Appl. Chem. 87 (9–10) (2015) 1051–1069, https://doi.org/10.1515/pac-2014-1117.

[45] J. Wang, S. Kaskel, KOH activation of carbon-based materials for energy storage, *J. Mater. Chem.*, 22(45) (2012) 23710–23725. 10.1039/c2jm34066f.

[46] Z. Zapata-Benabithe, G. Diossa, C.D. Castro, G. Quintana, Activated carbon bio-xerogels as electrodes for super capacitors applications, *Procedia Eng.*, (2016) 18–24. 10.1016/j.proeng.2016.06.470.

[47] E. Frackowiak, Carbon materials for supercapacitor application, PCCP 9 (15) (2007) 1774–1785, https://doi.org/10.1039/b618139m.

[48] A.G. Pandolfo, A.F. Hollenkamp, Carbon properties and their role in supercapacitors, *J. Power Sour.*, 157(1) (2006) 11–27. 10.1016/j.jpowsour.2006.02.065.

[49] E. R. Jr. Nightingale, phenomenological theory of ion solvation. Effective radii of hydrated ions, *J. Phys. Chem.*, 63(9) (1959) 1381–1387, 10.1021/j150579a011.

[50] B. Pal, S. Yang, S. Ramesh, V. Thangadurai, R. Jose, Electrolyte selection for supercapacitive devices: A critical review, Nanoscale Adv. 1 (10) (2019) 3807–3835, https://doi.org/10.1039/c9na00374f.

[51] G. Lin, R. Ma, Y. Zhou, Q. Liu, X. Dong, J. Wang, KOH activation of biomass-derived nitrogen-doped carbons for supercapacitor and electrocatalytic oxygen reduction, Electrochim. Acta 261 (2018) 49–57, https://doi.org/10.1016/j.electacta.2017.12.107.

[52] C. Zequine, et al., High-performance flexible supercapacitors obtained via recycled jute: bio-waste to energy storage approach, Sci. Rep. 7 (1) (2017), https://doi.org/10.1038/s41598-017-01319-w.

[53] K. Chaitra, et al., KOH activated carbon derived from biomass-banana fibers as an efficient negative electrode in high performance asymmetric supercapacitor, J. Energy Chem. 26 (1) (2017) 56–62, https://doi.org/10.1016/j.jechem.2016.07.003.

[54] H. Liu, et al., A sustainable one-step strategy for highly graphitized capacitive carbons with hierarchical micro-meso-macro porosity, Nanoscale Adv. 4 (5) (2022) 1394–1407, https://doi.org/10.1039/d1na00856k.

[55] L. Figueiredo, M. Pereira, M. Freitas, J. Orfaó, Modification of the surface chemistry of activated carbons. J. Carbons, (1999).

[56] A. Elmouwahidi, Z. Zapata-Benabithe, F. Carrasco-Marín, C. Moreno-Castilla, Activated carbons from KOH-activation of argan (Argania spinosa) seed shells as supercapacitor electrodes, Bioresour. Technol. 111 (2012) 185–190, https://doi.org/10.1016/j.biortech.2012.02.010.

[57] S. Ghosh, S.R. Polaki, P.K. Ajikumar, N.G. Krishna, M. Kamruddin, Aging effects on vertical graphene nanosheets and their thermal stability, Indian J. Phys. 92 (3) (2018) 337–342, https://doi.org/10.1007/s12648-017-1113-0.

[58] S. Ghosh, S. Barg, S. M. Jeong, K. Ostrikov, Heteroatom-doped and oxygen-functionalized nanocarbons for high-performance supercapacitors, *Adv. Energy Mater.*, 10(32) (2020). 10.1002/aenm.202001239.

[59] M. Winter, R.J. Brodd, What are batteries, fuel cells, and supercapacitors? Chem. Rev. 104 (10) (2004) 4245–4270, https://doi.org/10.1021/cr020730k.

[60] T. Lin *et al.*, Nitrogen-doped mesoporous carbon of extraordinary capacitance for electrochemical energy storage, *Science (1979)*, 350(6267) (2015) 1508–1513, 10.1126/science.aab3798.

[61] X. Qu, W. Kang, C. Lai, C. Zhang, S.W. Hong, A simple route to produce highly efficient porous carbons recycled from tea waste for high-performance symmetric supercapacitor electrodes, *Molecules*, 27(3) (2022), 10.3390/molecules27030791.

[62] X. Jing, et al., KOH chemical-activated porous carbon sponges for monolithic supercapacitor electrodes, ACS Appl. Energy Mater. 4 (7) (2021) 6768–6776, https://doi.org/10.1021/acsaem.1c00868.

[63] Z. Jovanovic, et al., The role of surface chemistry in the charge storage properties of graphene oxide, Electrochim. Acta 258 (2017) 1228–1243, https://doi.org/10.1016/j.electacta.2017.11.178.

[64] Y.-R. Nian, H. Teng, Nitric acid modification of activated carbon electrodes for improvement of electrochemical capacitance, J. Electrochem. Soc. 149 (8) (2002) A1008, https://doi.org/10.1149/1.1490535.

[65] H. Chen, et al., An activated carbon derived from tobacco waste for use as a supercapacitor electrode material, Xinxing Tan Cailiao/new Carbon Materials 32 (6) (2017) 592–599, https://doi.org/10.1016/S1872-5805(17)60140-9.
[66] M.J. Bleda-Martínez, D. Lozano-Castelló, E. Morallón, D. Cazorla-Amorós, A. Linares-Solano, Chemical and electrochemical characterization of porous carbon materials, Carbon N Y 44 (13) (2006) 2642–2651, https://doi.org/10.1016/j.carbon.2006.04.017.
[67] V. Sunil, B. Pal, I. Izwan Misnon, R. Jose, Characterization of supercapacitive charge storage device using electrochemical impedance spectroscopy, Mater. Today:. Proc. 46 (2021) 1588–1594, https://doi.org/10.1016/j.matpr.2020.07.248.
[68] B.-A. Mei, O. Munteshari, J. Lau, B. Dunn, L. Pilon, Physical interpretations of nyquist plots for EDLC electrodes and devices, J. Phys. Chem. C 122 (1) (2018) 194–206, https://doi.org/10.1021/acs.jpcc.7b10582.
[69] N.O. Laschuk, E.B. Easton, O.V. Zenkina, Reducing the resistance for the use of electrochemical impedance spectroscopy analysis in materials chemistry, RSC Adv. 11 (45) (2021) 27925–27936, https://doi.org/10.1039/D1RA03785D.
[70] M. Jerigová, M. Odziomek, N. López-Salas, 'We Are Here!' Oxygen functional groups in carbons for electrochemical applications, ACS Omega 7 (14) (2022) 11544–11554, https://doi.org/10.1021/acsomega.2c00639.